nature communications

Article

https://doi.org/10.1038/s41467-025-63684-9

Lattice-matched molecular-anchor design for high-performance perovskite quantum dot light-emitting diodes

Received: 15 April 2025

Accepted: 27 August 2025

Published online: 02 September 2025

Check for updates

Jiawei Chen[1,2,8], Xiangyu Liu[1,8], Bo Cai[3,8], Yuanzhuang Cheng[1], Hao Wen[4], Danlei Zhu[1], Yaonan Xiong[5], Linjie Dai[6], Xinghua Yan[1], Baixu Xiang[4], Xiyu Luo[1], Wenjing Feng[1], Jiuyao Du[1], Shuyue Dong[1], Qingsong Shan[2], Shulin Chen[5], Haibo Zeng[2], Qihua Xiong[4], Lian Duan[1,7] ✉ & Dongxin Ma[1,7] ✉

Perovskite quantum dot light-emitting diodes have rapidly achieved high external quantum efficiencies of over 25%; however, hindered by limited operating stability originating from surface defects or ion migration in quantum dots. Here, we design a lattice-matched anchoring molecule, tris(4-methoxyphenyl)phosphine oxide (TMeOPPO-*p*), to anchor the multi-site defects and stabilise the lattice. The target quantum dots exhibit high exciton recombination features with near-unity photoluminescence quantum yields (97%), and the as-fabricated quantum dot light-emitting diodes present a maximum external quantum efficiency of up to 27% at 693 nm, a low efficiency roll-off (over 20% at a current density of 100 mA cm^{-2} for the typical device) and an operating half-life of over 23,000 h. Besides, the air-processed devices maintain a maximum external quantum efficiency of over 26% with good storage stability. We expect this work to exert a profound influence on rational and on-demand molecule design for perovskite QDs, indicating great promise in optoelectronic applications.

Perovskite quantum dot light-emitting diodes (QLEDs) have made impressive progress for the past few years, achieving external quantum efficiencies (EQEs) of over 25% and exhibiting great potential in optoelectronic applications[1–5]. However, the operating stability of perovskite QLEDs still lags due to the defects inevitably generated during the purification process of quantum dots (QDs) and the resulting field-induced ion migration, further hampering their further development and industrialisation in high-definition displays and precise biomedical treatments[6–12].

For perovskite QDs, the surface ligands (e.g. oleyl amine, oleic acid) play a dual role in both protection and restriction. On the one hand, they serve as passivators to reduce surface defects, thereby improving the photoluminescence quantum yields (PLQYs) and stability of QDs. On the other hand, they usually possess poor electrical conductivity due to their long alkyl chains. Thus, too many surface ligands would block charge injection and transport in QLEDs[13–17]. Polar solvents are used to wash the extra ligands to achieve QDs with rational ligand density. However, partial ligands binding with the halogen atoms were

[1]Key Lab of Organic Optoelectronics and Molecular Engineering of Ministry of Education, Department of Chemistry, Tsinghua University, Beijing, China. [2]MIIT Key Laboratory of Advanced Display Materials and Devices, School of Materials Science and Engineering, Nanjing University of Science and Technology, Nanjing, China. [3]State Key Laboratory for Organic Electronics and Information Displays & Institute of Advanced Materials, Nanjing University of Posts & Telecommunications, Nanjing, China. [4]Department of Physics, Tsinghua University, Beijing, China. [5]Changsha Semiconductor Technology and Application Innovation Research Institute, College of Semiconductors (College of Integrated Circuits), Hunan University, Changsha, China. [6]Cavendish Laboratory, University of Cambridge, Cambridge, UK. [7]State Key Laboratory of Flexible Electronics Technology, Tsinghua University, Beijing, China. [8]These authors contributed equally: Jiawei Chen, Xiangyu Liu, Bo Cai. ✉e-mail: duanl@mail.tsinghua.edu.cn; dongxinma@mail.tsinghua.edu.cn

accidentally removed by polar solvents, resulting in halide vacancies or uncoordinated Pb^{2+}, which would act as surface defects and ion migration channels, thereby degrading device performance[1,3,18,19].

In order to solve the problem, researchers proposed a series of additives with passivating groups, such as phosphine oxide (P=O), sulfur oxide (S=O), carboxide (C=O), etc[20,21]. These functional groups have strong interactions with the surface uncoordinated Pb^{2+} and thus prevent the ion migration in the electric field[8,22]. However, the reported molecules generally have only one binding site or multiple lattice-mismatched binding sites. Due to the large space steric hindrance, these large-sized molecules can not approach close enough to the perovskite lattice and thus can not offer a strong interaction or sufficient passivation[23–25].

In this work, we propose a lattice-matched molecular anchoring strategy by using tris(4-methoxyphenyl)phosphine oxide (TMeOPPO-*p*) for efficient and stable QLEDs. The electron-donating P=O and -OCH_3 groups in TMeOPPO-*p* could interact strongly with uncoordinated Pb^{2+}, and the interatomic distance of the O atoms is 6.5 Å, matching the lattice spacing of QDs (also 6.5 Å) and offering multi-site anchoring interaction. Thus, the target QDs exhibit high exciton recombination features with a PLQY of 97%, and the as-fabricated QLED presents a maximum EQE of 26.91% and good stability with an operating lifetime of over 23,000 h. Typical QLEDs exhibit a very small efficiency roll-off, i.e. an EQE of over 20% at a current density of 100 mA cm^{-2}. Additionally, the air-processed QLEDs exhibit a maximum EQE of 26.28%, demonstrating the oxygen and water resistance of the QDs. Our work gives an insight into designing passivating molecules conforming to perovskite lattice properties and provides the possibility of unplugging a future practical application bottleneck.

Results

Lattice-matched anchoring molecule design

We first conducted a precise molecule design to match the molecular anchor and perovskite lattice accurately. To enable the molecule to have interfacial anchoring properties, we attempted multi-site substitution of the molecule. We chose triphenylphosphine oxide (TPPO) as the basic molecular framework. The calculated interatomic distance of the O atoms from the P=O and the phenyl ring's ortho, meta, and para positions was 3.1 Å, 4.4 Å and 5.3 Å, respectively. To study the effect of site spacing and nucleophilicity on QDs, we synthesised a series of multi-site anchoring molecules, including TMeOPPO-*o*, TMeOPPO-*p*, TFPPO, TClPPO, and TBrPPO (Fig. 1a). The site spacing of multi-site anchoring molecules in that order is 2.6 Å, 6.5 Å, 6.6 Å, 7.0 Å and 7.2 Å, respectively. The TMeOPPO-*p* could precisely match the lattice spacing of QDs, allowing it to attach to the surface of the perovskite lattice and provide adequate passivation (Fig. 1b)[26]. Besides, the nucleophilicity of -OCH_3, F^-, Cl^- and Br^- decreases in turn, according to the calculated electrostatic potential results (Supplementary Data 1). Additionally, the triple-attached nucleophilic groups significantly increase their probability of interacting with uncoordinated Pb^{2+}.

We then calculated the projected density of states (PDOSs) of the QDs to further verify the proposed lattice-matched multi-site anchoring effect (Supplementary Fig. 1)[21]. The calculated PDOS revealed that the pristine QDs possess imperfect surface sites featuring a conspicuous trap state originating from halide vacancies or uncoordinated Pb^{2+} $6p_z$ orbital (Fig. 1c). We then calculated the PDOSs of single-site anchored (TPPO-treated) QDs. The Pb-$6p_z$ trap states around the Fermi level were eliminated entirely by O-2*p*, whereas the uncoordinated Pb^{2+} maintained the trap states. Meanwhile, the trap peaks were separated from the conduction band minimum (CBM) state, showing that the consecutive trap states could not be eliminated sufficiently (Fig. 1d). When the TMeOPPO-*p* offered lattice-matched multi-site anchoring interaction, the trap states and the CBM peaks connected completely, revealing that the P=O and -OCH_3 groups from TMeOPPO-*p* could strongly interact with uncoordinated Pb^{2+}, stabilise the lattice and eliminate the trap states entirely (Fig. 1e)[27]. Notably, when the difference between the site spacing of groups and perovskite lattice is too large (i.e. TMeOPPO-*o*), enforced coordination will instead introduce substantial strain, leading to severe structural distortion after optimisation—manifested by anomalous phenomena such as the transformation of benzene rings into five-membered rings. In mismatched multi-site models, failure to enforce passivation at every site results in passivation effects analogous to those in single-site models.

Microstructural and surface chemical properties

We synthesised the perovskite $CsPbI_3$ QDs by using a modified hot-injection method[26]. Details of the synthesis and purification process are provided in the Methods. We first compared the average PLQYs of QD solutions treated with different molecules (concentration of 5 mg mL^{-1} in ethyl acetate). The pristine QD and QDs treated with TPPO, TMeOPPO-*o*, TMeOPPO-*p*, TFPPO, TClPPO, and TBrPPO showed average PLQYs of 59%, 70%, 82%, 96%, 92%, 88%, and 87%, respectively (Fig. 2a and Supplementary Fig. 2). The QDs treated with TMeOPPO-*p* showed the highest PLQYs, which is consistent with the theoretical calculation results. TMeOPPO-*p* could offer multi-site anchoring interactions and eliminate defects in QDs (Fig. 2b); thus, it is designated as the representative molecule for further exploration.

Then, we characterised the microstructures of QDs by using the aberration-corrected scanning transmission electron microscope (STEM) and X-ray diffraction (XRD) measurements. The estimated lattice spacings of the pristine and target QDs were both 6.5 Å. The pristine QDs presented uneven crystal sizes resulting from QD decomposition or ripening, whereas the target ones exhibited uniform and cubic morphologies with clear lattice fringes, indicating good crystallinity (Fig. 2c)[26,28]. The typical diffraction peaks in the XRD results indicated the cubic phase structure of the pristine QD film[29]. We observed neither additional diffraction peaks nor obvious location and shape of main diffraction peaks in the target QD film, suggesting that TMeOPPO-*p* did not change the crystalline structure of QDs (Fig. 2d)[30].

To better understand the interaction between TMeOPPO-*p* and QDs, we employed Fourier transform infrared (FTIR) spectroscopy, X-ray photoelectron spectroscopy (XPS), and nuclear magnetic resonance (NMR) measurements. The C–H stretching modes (2700-3000 cm^{-1}) from oleyl amine /oleic acid ligands were weakened in target QDs (Fig. 2e), indicating that TMeOPPO-*p* could partially connect with the uncoordinated Pb^{2+}, thus avoiding the weak and dynamic connection between ligands and QDs. In XPS results, the characteristic peaks of Pb 4*f* from the target QDs shifted to lower binding energies compared to peaks from the pristine QDs (Fig. 2f), which could be ascribed to the interaction between TMeOPPO-*p* and QDs enhancing the shielding effect between inner electrons and the Pb nucleus[31,32]. In the ^{1}H NMR spectra of TMeOPPO-*p*, there was a sharp peak corresponding to the methoxy group (-OCH_3) at δ 3.81, and we also observed a peak at a similar position in the target QDs (Fig. 2g). The presence of TMeOPPO-*p* in the target QDs was also proved in the ^{31}P NMR spectra. However, there were neither ^{1}H (from -OCH_3) nor ^{31}P (from P=O) NMR signals in the pristine QDs, suggesting that TMeOPPO-*p* could interact with QDs and end up on the QD surface (Fig. 2h). Notably, the ^{1}H NMR spectra of the target QDs showed a higher chemical shift, while the ^{31}P NMR spectra of the target QDs showed a lower chemical shift. The P=O bond in TMeOPPO-*p* coordinated with Pb^{2+} in the form of a double bond. This process not only formed a sigma coordination bond but also allowed the d orbitals of the Pb atom to interact with the π*-antibonding orbital of the double bond, creating a π backbonding. This delocalised the charge on the Pb and increased the π-electron density, thereby slightly shifting the ^{31}P NMR peak upfield. In contrast, when the methoxy group is bound to Pb, no π backbonding was formed, resulting in a reduction of the electron cloud density around the hydrogen atoms and a downfield shift in the ^{1}H NMR peak. In brief, the FTIR, XPS and NMR results all

https://doi.org/10.1038/s41467-025-63684-9

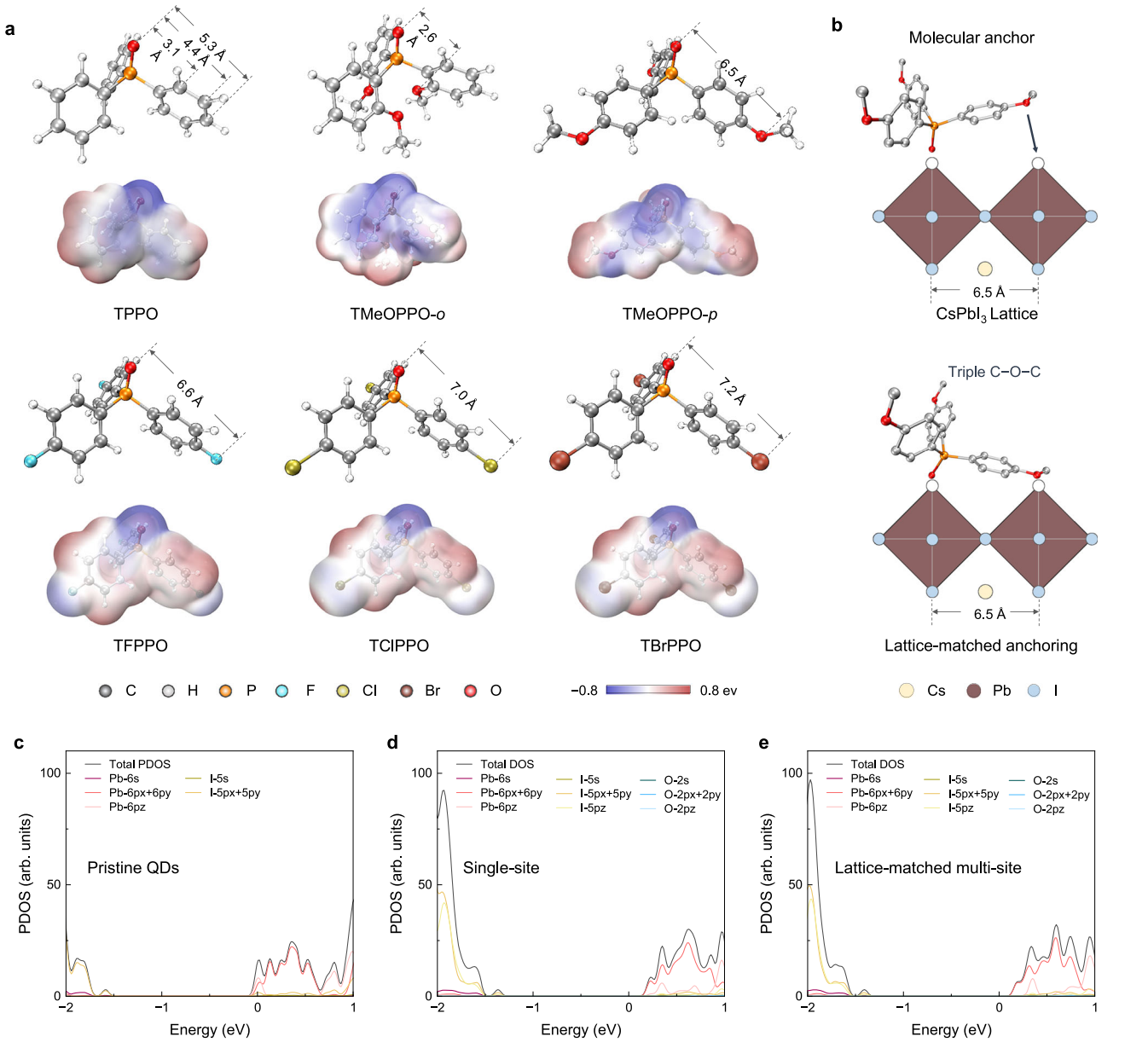

Fig. 1 | Lattice-matched multi-site-anchoring strategy. a Schematic illustration of lattice-matched anchoring molecule design and the corresponding calculated electrostatic potential results. **b** Schematic illustration of the lattice-matched molecular anchoring effect. **c** PDOS of the perovskite QDs with surface defects. **d** PDOS of the perovskite QDs treated with the single-site molecule. **e** PDOS of the perovskite QDs with multi-site lattice-matched anchoring effect.

proved that TMeOPPO-*p* could strongly interact with the surface of QDs, which is consistent with the theoretical calculations above.

Optical properties and exciton dynamics

Compared to the pristine ones, the target QDs showed enhanced and red-shifted photoluminescence (PL) emission with a full width at half maximum (FWHM) of 32 nm (Fig. 3a). The PLQY was 97%, much higher than the pristine QDs (65%). Time-resolved photoluminescence (TRPL) decay results (Fig. 3b) showed that the target QDs presented a longer average carrier lifetime (τ_{avg}) compared with the pristine ones, increasing from 8.22 ns to 19.17 ns (see Supplementary Table 1 for the fitting details). Besides, the trap-related fast decay component was reduced from 0.67 to 0.37, suggesting the suppressed trap states in the target QDs.

We applied ultrafast transient absorption (TA) spectroscopy to investigate the difference in the electron evolution process between the pristine and target QD solutions. The ground state bleach (GSB) dynamics of the QD samples at low fluence (0.61 μJ cm^{-2}) were presented in Fig. 3c, with corresponding TA maps and spectra provided in Supplementary Fig. 3. Both samples exhibited an initial decay, followed by a slower component of great similarity. The initial drop in GSB was attributed to the trapping of photoexcitations within the QDs, while the subsequent slow decay corresponded to the intrinsic recombination of the material. Notably, the target QDs demonstrated significantly reduced trapping compared to control QDs, which is consistent with the PL and PLQY results. All these results above indicate that the defects were effectively eliminated, and the trap-related nonradiative recombination was suppressed in the target QDs.

We next fabricated thin films of the QDs and investigated the effects of TMeOPPO-*p* on the film-forming property by using scanning electron microscopy (SEM) and atomic force microscopy (AFM). Both the pristine and target QDs can completely cover the substrate, as presented in Supplementary Fig. 4. Although the target QDs showed lower surface ligand density, no slight aggregations were observed. Besides, the target QD film was smoother than the pristine one, with a

https://doi.org/10.1038/s41467-025-63684-9

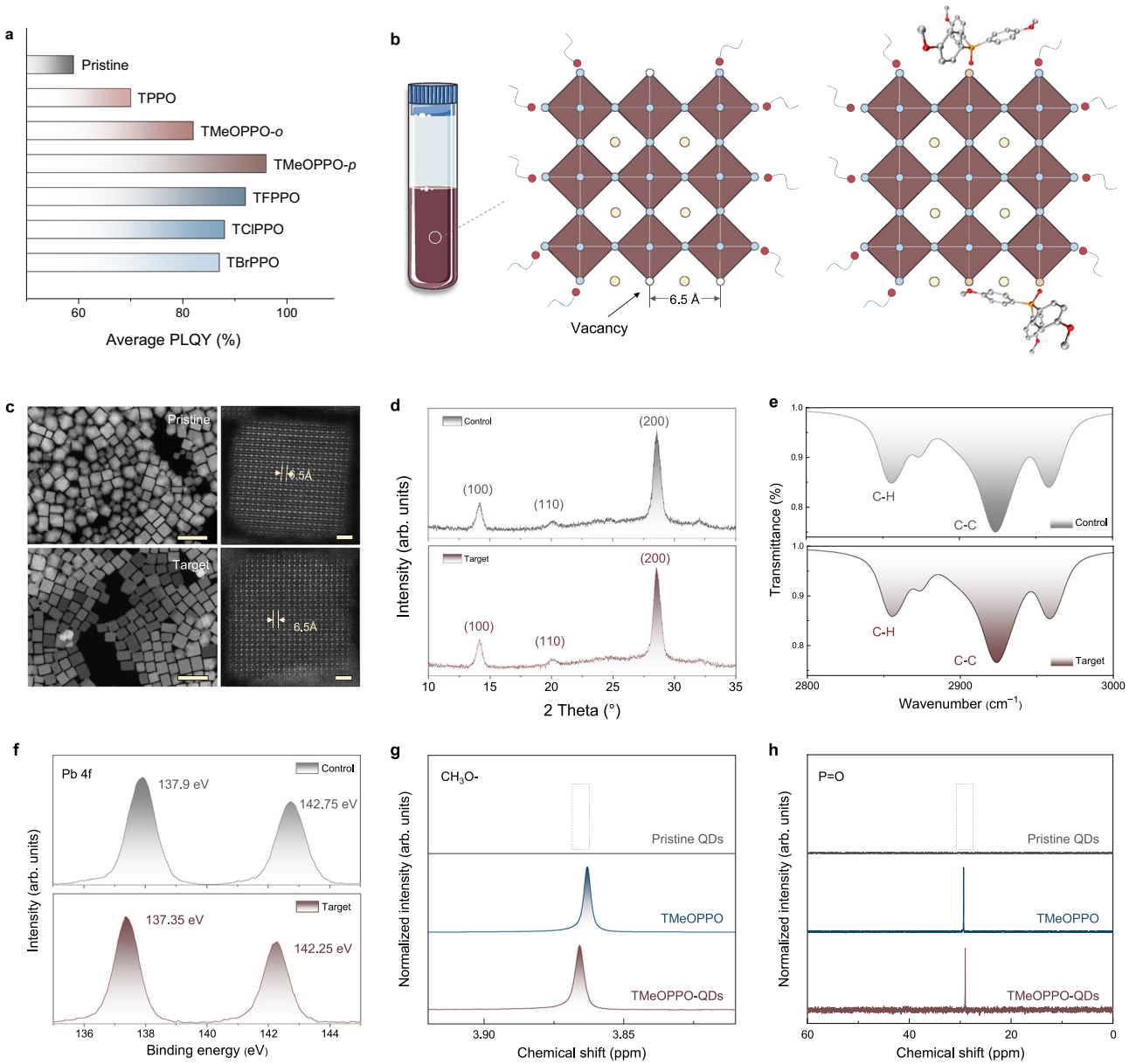

Fig. 2 | Microstructural and surface chemical properties. a Average PLQYs of QD solution treated by different molecules. **b** Schematic illustration of anchoring effect on $CsPbI_3$ QDs. **c** STEM images of the pristine and target QDs. Scale bars, 50 nm (the left column) and 2 nm (the right column). **d** XRD patterns of the pristine and target QD films. **e** FTIR spectra of the QDs. **f** XPS spectra of Pb 4*f* of the QD films. **g** ^{1}H NMR spectra of the pristine QDs, TMeOPPO-*p*, and target QDs. **h** ^{31}P NMR spectra of the pristine QDs, TMeOPPO-*p*, and target QDs.

root-mean-square roughness (*R*q) value of 4.43 nm (Supplementary Fig. 5, *R*q value is 5.13 nm for the pristine one). We applied space-charge-limited current (SCLC) measurements to confirm the electrical properties and trap states of these QD films. We fabricated hole-only devices with the configuration of indium tin oxide (ITO)/ poly(-ethylene dioxythiophene): polystyrene sulfonate doped with nafion perfluorinated ionomer (PEDOT: PSS: PFI)/ poly[bis(4-phenyl)(2,4,6-trimethylphenyl)amine] (PTAA)/ QD film/ molybdenum trioxide (MoO_x)/ Al (Fig. 3d). The trap-filled limit voltages (V_{TFL}) of the control and target devices were determined to be 0.71 V and 0.45 V, respectively (Fig. 3e, f). By using equation $N = 2\varepsilon_0\varepsilon_r V_{TFL}/eL^2$ [19,33], the calculated hole trap densities of the control and target devices were $1.06 \times 10^{18}\,cm^{-3}$ and $6.69 \times 10^{17}\,cm^{-3}$, respectively. These results represented good film-forming properties and reduced trap states of the target QDs, which laid a solid groundwork for constructing high-performance devices.

Performance of perovskite QLEDs

Based on these high-quality perovskite QD films, we fabricated QLEDs with an ITO/ PEDOT: PSS: PFI/ PTAA/ QD film/ TPBi/ LiF/ Al architecture (Fig. 4a–c). The target QLED exhibited a lower turn-on voltage and a higher current density than the control device (Supplementary Fig. 6 and Fig. 4d), which can be attributed to the improved carrier transport characteristics. The radiance of the target QLED increased rapidly with the increase in voltage, yielding a maximum radiance of 119,037 mW Sr m^{-2}, a threefold improvement over the control device (Fig. 4e).

Benefiting from the reduced trap states and enhanced exciton recombination, the target QLED showed an efficiency boost. The maximal EQE of the target QLED reached 26.91% with optimised concentrations of TMeOPPO-*p* in ethyl acetate (Supplementary Fig. 7), achieving a considerable improvement compared to the control device (Fig. 4f). The EQE histogram of 30 devices was presented in Fig. 4g, showing an average EQE of 25.3% with high reproducibility. As

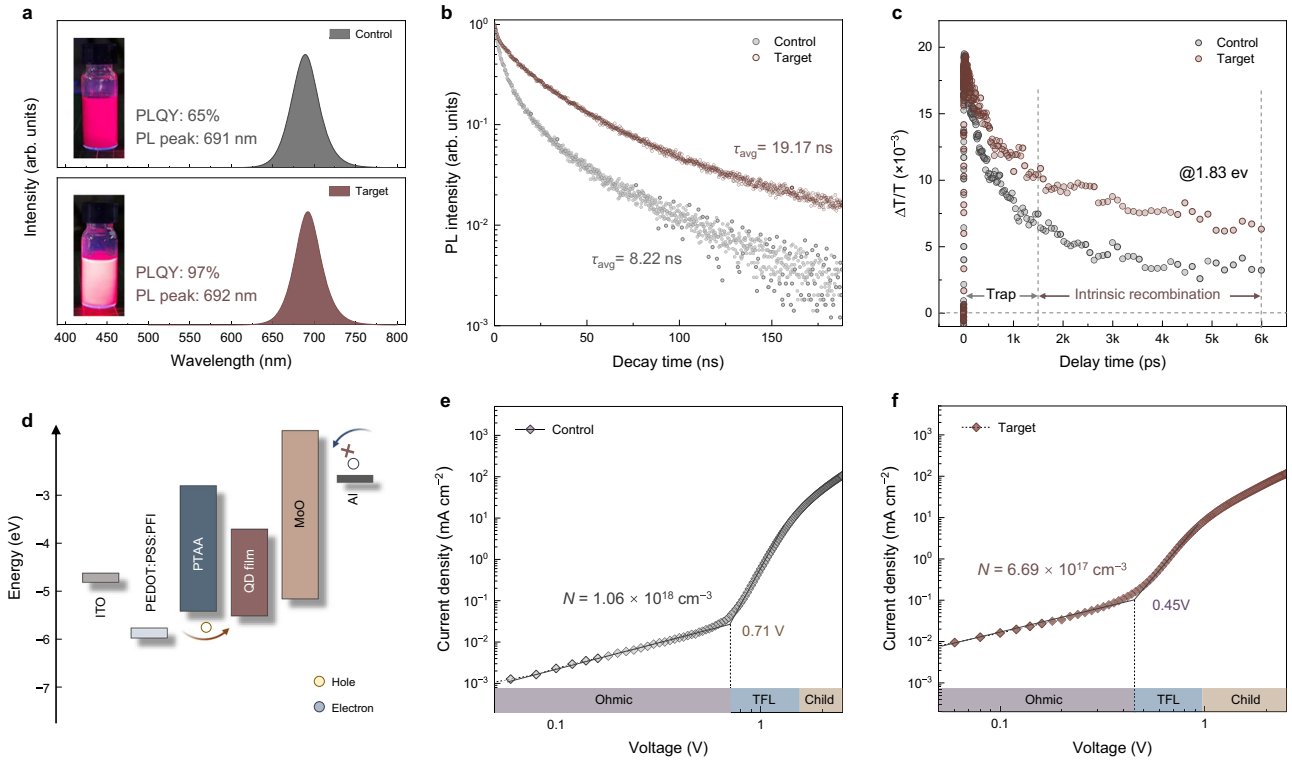

Fig. 3 | Optical and electrical properties. a PL spectra and the photographs of the $CsPbI_3$ QD solutions under the UV lamp. **b** TRPL curves of the QDs. **c** GSB kinetics at 1.83 eV extracted from transient TA measurements for pristine and target QDs under low fluence (2.14 eV, 0.61 μJ cm^{-2}). **d** Energy diagram of the hole-only devices. **e** Current-voltage characteristics of the control hole-only device. **f** Current-voltage characteristics of the target hole-only device.

presented in Fig. 4h, i, the control QLED exhibited the EL peak centred at 691 nm with an FWHM of 33 nm, corresponding to the CIE coordinates of (0.72, 0.27), while the target one showed a 2 nm red-shifted EL spectrum and corresponding CIE coordinates (0.73, 0.27), which were consistent with PL results.

Stability of perovskite QLEDs

Apart from enhancing exciton recombination (e.g. higher EQE and radiance), our strategy can also improve the stability of the devices. We first evaluated the operating stability of the target QLED. We individually tested the radiance decays of the control and target devices under varying initial radiance levels. Here, we estimated the T_{50} through an empirical scaling law widely used for simulating LED degradation:

$$R_0^{\,n} T_{50} = constant \quad (1)$$

Where n is the acceleration factor[34,35], and the value was obtained by fitting T_{50} under different initial radiance. We calculated that the values of n are both 1.87 and the T_{50} for the control and target devices could be estimated to be 1350 h and 23,420 h (Fig. 5a, b and Supplementary Fig. 8), respectively, at an initial radiance of 190 mW Sr^{-1} m^{-2} (corresponding to a luminance of 100 cd m^{-2} for green perovskite LED with EL peak centred at 525 nm, see Supplementary Fig. 9 for details).

Then, we compared the characteristics of the target QLED with the reported red perovskite LEDs (EL peaked at 600-700 nm), as shown in Fig. 5c[1,36,37]. Our work presented an ultra-high EQE of over 25% while keeping a remarkable lifetime of over 23,000 h. Benefiting from the stabilised lattice and inhibited ion migration in QDs, the target QLEDs show ultra-low efficiency roll-off at high current densities. The EQE of the target QLED remained over 15% under 100 mA cm^{-2} (even over 20% for the typical QLED shown in Supplementary Fig. 10), while the EQEs of other reported perovskite LEDs dropped below 10%, even below 3%.

Finally, we fabricated air-processed QLEDs, i.e. spin-coating PEDOT: PSS: PFI, PTAA and QD solution in ambient air, followed by a vacuum evaporation process. The air-processed QLED exhibited a maximum radiance of 74,356 mW Sr^{-1} m^{-2}, a maximum EQE of 26.28% and no EL shift, indicating good oxygen and water resistance and practical application potential for solution processing techniques (Fig. 5d–f and Supplementary Fig. 11). Besides, the typical air-processed QLED demonstrated good storage stability, which can be attributed to the complete elimination of defects that enhance the water and oxygen resistance of QDs (Fig. 5g–i). In brief, the target QLEDs not only possessed outstanding electro-optical conversion characteristics but also demonstrated excellent stability in water-oxygen environments, under continuous operation, or at high current densities (Supplementary Fig. 11 and Supplementary Table 2).

The superiority of lattice-matched molecular-anchor

To represent the universal effect of phosphine oxide molecules and highlight the superiority of our lattice-matched multi-site anchoring strategy, here we compared the effects of other designed molecules, including TPPO, TMeOPPO-*o*, TFPPO, TClPPO and TBrPPO. Compared with the control one, the as-fabricated QLEDs presented improved performance of different magnitudes (Fig. 6 and Supplementary Fig. 12). For example, the devices based on the QDs treated with TPPO, TMeOPPO-*o*, TFPPO, TClPPO and TBrPPO achieved the highest radiance of 49,018 mW Sr m^{-2}, 54,821 mW Sr m^{-2}, 67,410 mW Sr m^{-2}, 85,859 mW Sr m^{-2} and 69,587 mW Sr m^{-2}, respectively. The maximum EQEs in that order were 19.79%, 20.16%, 23.62%, 22.38% and 21.45%, respectively. For operating stability, we calculated that the values of n are 1.87, 1.87, 1.87, 1.86, and 1.86 for the devices based on the TPPO-, TMeOPPO-*o*-, TFPPO-, TClPPO- and TBrPPO-treated QDs, respectively. The T_{50} of the devices in that order could be estimated to be 1944 h, 3127 h, 8307 h, 6139 h and 4767 h, respectively.

https://doi.org/10.1038/s41467-025-63684-9

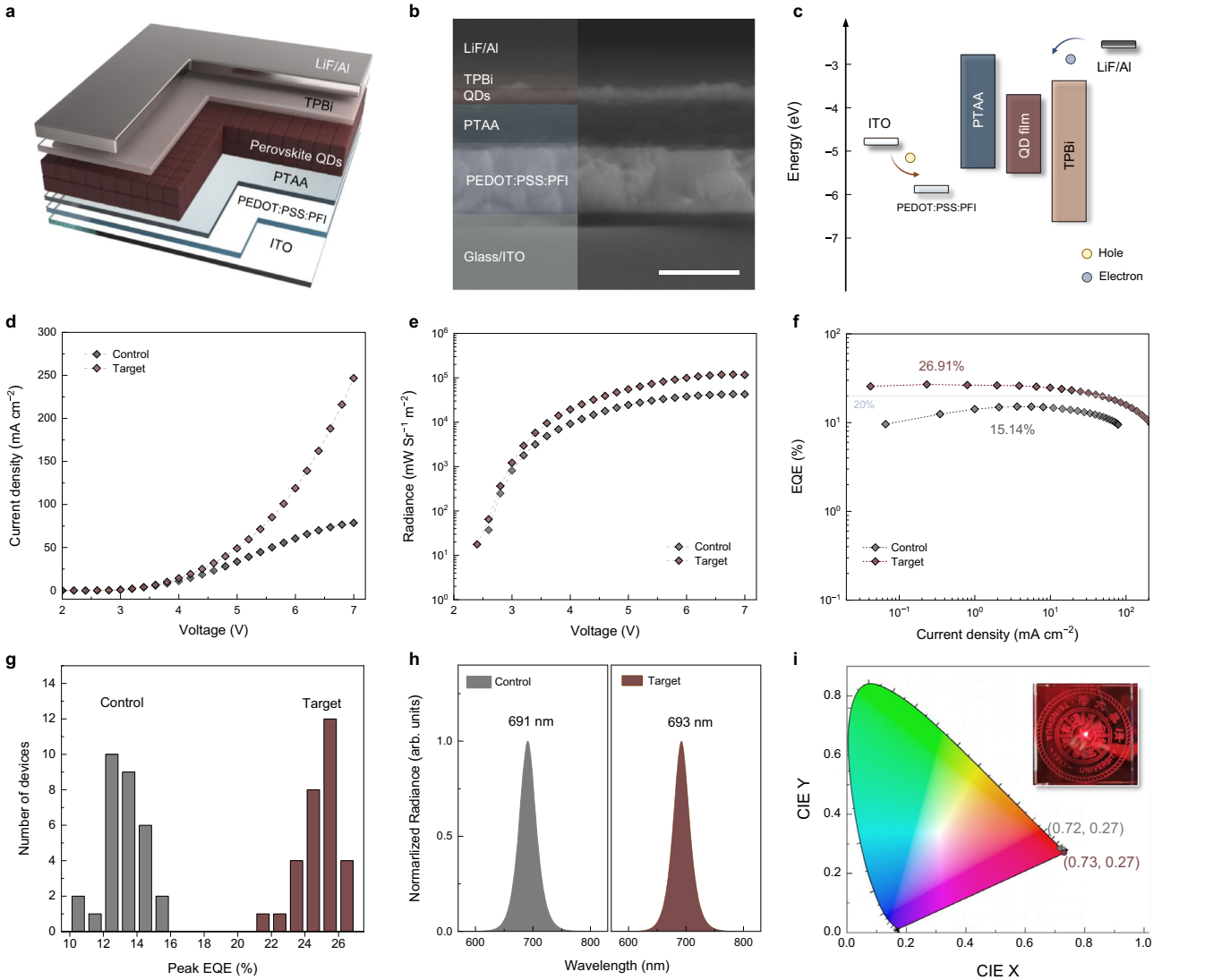

Fig. 4 | Device performance. a Schematic illustration of the device structure. **b** The cross-sectional SEM image of the target QLED. Scale bar, 200 nm. **c** Energy diagram of the QLED. **d** Current density-voltage curves. **e** Radiance-voltage curves. **f** EQE curves. **g** The statistics of the distribution of max EQE of 30 devices for the pristine and target QLEDs. **h** EL spectra. **i** CIE diagram. The insert shows a photograph of the operating target device, illuminating the Tsinghua University logo.

We summarised all device performance parameters in Table 1. Combining the results of theoretical calculations, PLQYs, and device performance, we can draw the following conclusions: the site spacing and nucleophilicity of groups are the two key factors that affect the performance of QDs. The closer the site spacing is to the perovskite lattice spacing and the stronger nucleophilicity of the groups, the more stable the lattice and the fewer defects in QDs can be achieved, thereby facilitating the fabrication of more efficient and stable QLEDs.

Discussion

In summary, we have proposed a lattice-matched multi-site anchoring strategy by using TMeOPPO-*p* for high-efficiency and stable QLEDs. The TMeOPPO-*p* could match the lattice, adhere to the surface of $CsPbI_3$ QDs, and provide adequate multiple anchoring sites, which was further confirmed by DFT calculation results and surface chemical state information. The target QDs exhibited high exciton recombination features with a PLQY of 97%, enabling high-performance QLEDs with a maximum EQE of 26.91%, an ultra-low efficiency roll-off, an operating lifetime of over 23,000 h, and excellent oxygen and water resistance. The superiority of the lattice-matched multi-site anchoring strategy was demonstrated by comparing it with other lattice-mismatched anchoring molecules. Our results reveal the molecule design principles for eliminating multi-site defects synergistically and maximising the performance of QLED.

Methods

Materials

oleyl amine (OAm, 80-90% purity), oleic acid (OA, 80-90% purity), 1-octadecene (ODE, >80% purity), isopropanol (99.7% purity), ethyl acetate (99% purity) and toluene (≥99.5% purity) were supplied by Aladdin. Caesium stearate (CsSt, 98% purity) was supplied by J&K. N-octane (>98% purity) was supplied by TCI. Nafion perfluorinated ionomer (PFI, tetrafluoroethylene-perfluoro-3, 6-dioxa-4-methyl-7-octenesulfonic acid copolymer) was supplied by Sigma-Aldrich. Lead iodide (PbI_2, 99.99%), PEDOT: PSS (Baytron P VPAl 4083), TPBi and PTAA were supplied by Xi'an Yuri Solar Co., Ltd. Dichloromethane was supplied by Shanghai Titan Scientific Co., Ltd.

Synthesis of $CsPbI_3$ QD solution

We synthesised the QD solution referencing our previous report[26]. The caesium precursor was synthesised by mixing CsSt (2.5 g, 6 mmol), OA

https://doi.org/10.1038/s41467-025-63684-9

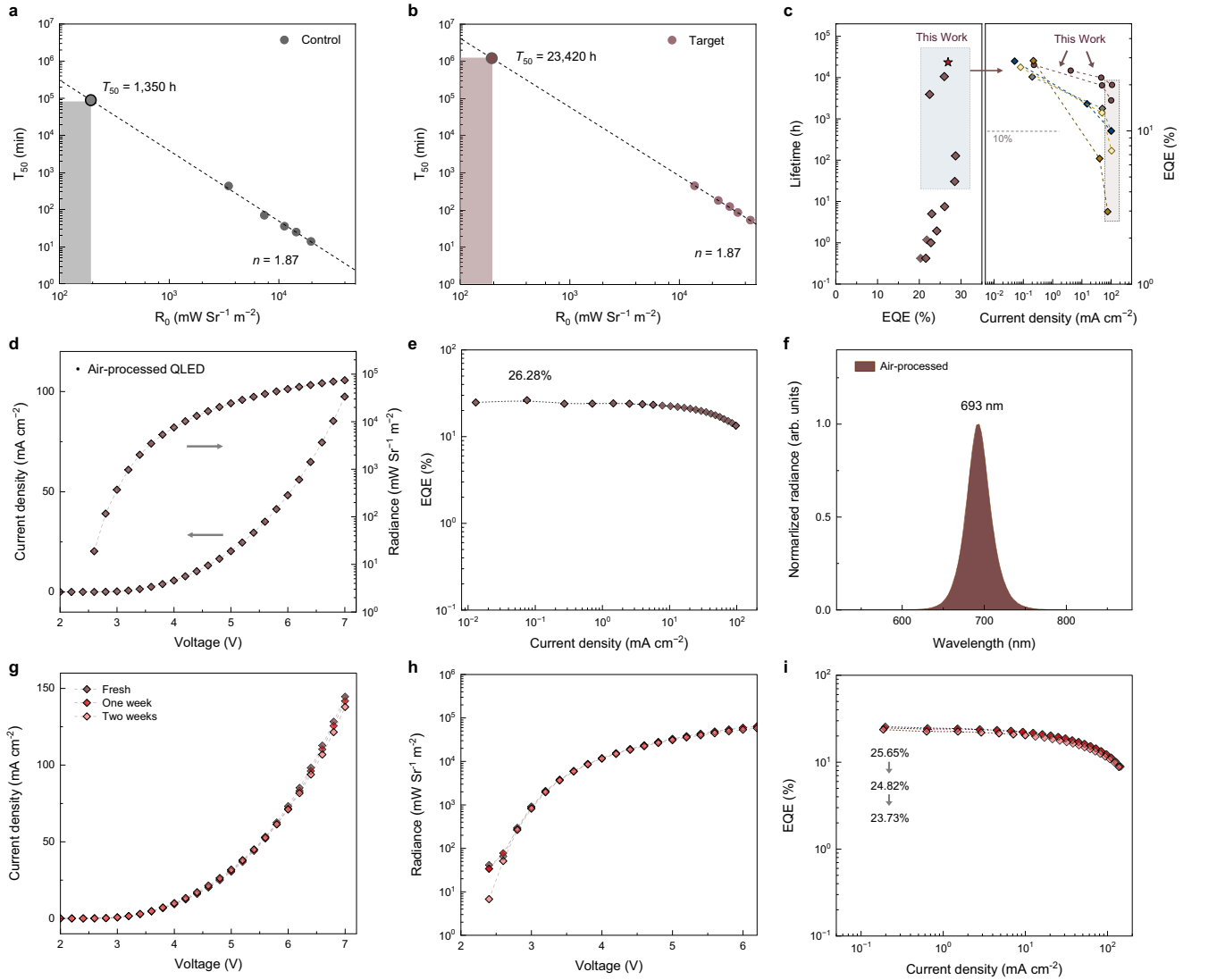

Fig. 5 | Stability of QLEDs. The T_{50} lifetimes as a function of R_0 for the control and target QLEDs. The dashed line fits the T_{50} data to the equation $R_0^n T_{50}$ = Constant, where n is the acceleration factor. **a** the control device. **b** the target device. **c** Summary of the reported red perovskite LED characteristics based on maximum EQE, T_{50} and roll-off. **d**–**f** EL performance of air-processed champion QLED. **d** Current density-voltage-radiance curve. **e** EQE curve. **f** EL spectra. **g**–**i** The storage stability of a typical air-processed QLED. **g** Current density-voltage curves of QLED after 0/1/2 weeks of storage. **h** Voltage-radiance curves of QLED after 0/1/2 weeks of storage. **i** EQE curves of QLED after 0/1/2 weeks of storage.

(2 mL) and ODE (40 mL). The mixture was then heated to 140 °C under continuous stirring until complete dissolution was achieved, as indicated by the formation of a homogeneous and transparent liquid. For pristine $CsPbI_3$ QDs, PbI_2 (0.25 g, 0.6 mmol), ODE (10.0 mL), OAm (1.5 mL) and OA (2.0 mL) were added into a 100 mL three-neck flask. The mixture was degassed at 120 °C for 5 min under nitrogen flow to remove oxygen and moisture. The temperature was raised to 180 °C to ensure the full solubilisation of PbI_2. Then, 1.0 mL of caesium precursor was quickly injected into the solution for a 15 s reaction. The flask was immediately immersed in an ice-water bath to quench the reaction and cool the solution to ambient temperature.

For the first-round purification process, the crude QD solution was transferred to centrifuge tubes, and then isopropanol with a 1:3 volume ratio was added, followed by centrifugation at 8000 × *g* for 1 min. The collected precipitate was dispersed in the toluene solution with a volume ratio of 1:1. For the second-round purification process, OAmI in toluene (0.05 mol L^{-1}) was added to a volume of 0.4 mL. Next, ethyl acetate was added to the solution in a 1:2 volume ratio, followed by centrifugation at 8000 × *g* for 1 min. The collected precipitate was then dispersed in *n*-octane. For treated QDs, different molecules (TPPO, TMeOPPO-*o*, TMeOPPO-*p*, TFPPO, TClPPO, and TBrPPO) in ethyl acetate (5 mg mL^{-1}) were added into the solution with a volume ratio of 1:2 during the second-round purification process. The remaining steps were the same.

Synthesis of a series of molecules

General procedure: The substituted triphenylphosphine (1.0 eq.) was dissolved in the THF (3.0 mL). A hydrogen peroxide solution in H_2O (30%, 5.0 eq.) was added dropwise and stirred for one hour at ambient temperature. After the reaction was quenched by saturated sodium thiosulfate ($Na_2S_2O_3$) solution, the organic phase was extracted with DCM. The solvent was removed under reduced pressure and the residue was recrystallised twice in the mixed solvent of DCM and hexane to get the final product for further use.

Trisphenylphosphine oxide (TPPO) was isolated as a white solid (120 mg, yield: 75%). mp: 155–156 °C (lit.ref 155–157 °C). ^{1}H NMR ($CDCl_3$, 400 MHz): δ 7.55–7.42 (m, 6H), 6.97 (t, *J* = 7.5, 3H), 6.90 (dd, *J* = 5.3, 2.3 Hz, 3H), 3.56 (s, 9H). ^{13}C NMR ($CDCl_3$, 100 MHz). δ 161.3, 134.0,

https://doi.org/10.1038/s41467-025-63684-9

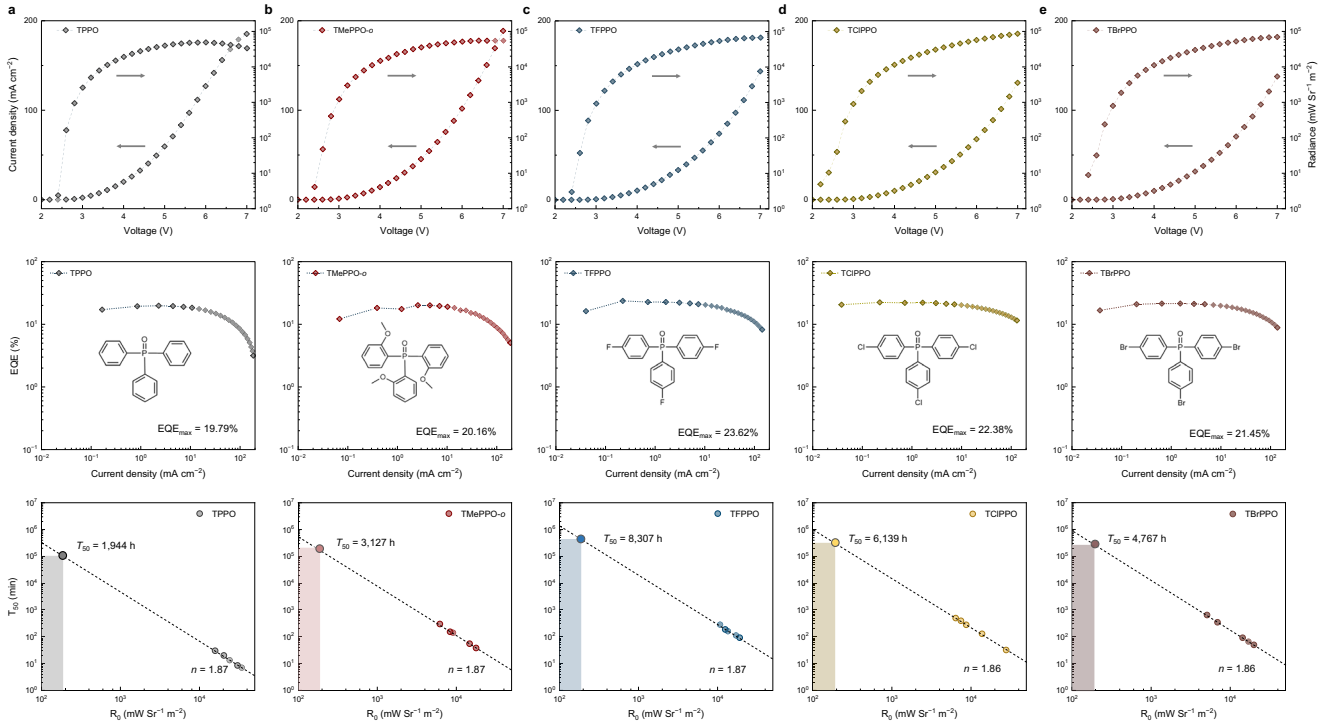

Fig. 6 | Performance of QLEDs by using various designed molecules. Electro-optical performance and stability of QLEDs by using various designed molecules, containing current density-radiance-voltage curve, EQE curve (the insert is the chemical structure) and operating stability. **a** TPPO. **b** TMeOPPO-*o*. **c** TFPPO. **d** TClPPO. **e** TBrPPO.

Table 1 | Device performance of QLEDs treated with different molecules

Device	Type		Radiance (mW Sr^{-1} m^{-2})	EQE$_{max}$ (%)	EQE$_{average}$ (%)	T_{50} (h)
Control	/	/	42,809 @6.8 V	15.14	12.8	1350
TPPO	Single-site	/	49,018 @6.0 V	19.79	17.7	1944
TMeOPPO-*o*	Multi-site	Lattice-mismatched	54,821 @7.0 V	20.16	19.4	3127
TMeOPPO-*p*	Multi-site	Lattice-matched	119,037 @6.8 V	26.91	25.3	23,420
TFPPO	Multi-site	Lattice-matched	67,410 @7.0 V	23.62	21.8	8307
TClPPO	Multi-site	Lattice-mismatched	85,859 @7.0 V	22.38	20.3	6139
TBrPPO	Multi-site	Lattice-mismatched	69,587 @7.0 V	21.45	19.6	4767

133.6, 121.2. ^{31}P NMR ($CDCl_3$, 162 MHz): δ 25.8. HRMS (m/z): $[M]^+$ calcd. for $C_{18}H_{15}OP$, 278.0861; found, 278.0868.

Tris(2-methoxyphenyl)phosphine oxide (TMeOPPO-*o*) was isolated as a white solid (115 mg, yield: 80%). mp: 203–205 °C (lit.ref 205–206 °C). ^{1}H NMR ($CDCl_3$, 400 MHz): δ 7.55–7.42 (m, 6H), 6.97 (t, J = 7.5, 3H), 6.90 (dd, J = 5.3, 2.3 Hz, 3H), 3.56 (s, 9H). ^{13}C NMR ($CDCl_3$, 100 MHz). δ 161.3, 134.0, 133.6, 121.2. ^{31}P NMR ($CDCl_3$, 162 MHz): δ 25.8. HRMS (m/z): $[M]^+$ calcd. for $C_{21}H_{21}O_4P$, 368.1177; found, 368.1182.

Tris(4-methoxyphenyl)phosphine oxide (TMeOPPO-*p*) was isolated as a white solid (106 mg, yield: 94%); mp: 143–145 °C (lit.ref 147–149 °C). ^{1}H NMR ($CDCl_3$, 400 MHz): δ 7.56 (dd, J = 8.8 Hz, J = 11.2 Hz, 6H), 6.95–6.93 (m, 6H), 3.81 (s, 9H). ^{13}C NMR ($CDCl_3$, 100 MHz): δ 162.2, 133.7, 124.2, 114.0, 55.3. ^{31}P NMR ($CDCl_3$, 162 MHz): δ 29.23. HRMS (m/z): $[M]^+$ calcd. for $C_{21}H_{21}O_4P$, 368.1177; found, 368.1183.

Tris(4-fluorophenyl)phosphine oxide (TFPPO) was isolated as a white solid (120 mg, yield: 91%). mp: 119–121 °C (lit.ref 120–121 °C). ^{1}H NMR ($CDCl_3$, 400 MHz): δ 7.67–7.60 (m, 6H), 7.19–7.15 (m, 6H). ^{13}C NMR ($CDCl_3$, 100 MHz): δ 165.2, 134.5, 128.2, 116.1. ^{31}P NMR ($CDCl_3$, 162 MHz): δ 26.9. ^{19}F NMR ($CDCl_3$, 376 MHz): δ–106.0. HRMS (m/z): $[M]^+$ calcd. for $C_{18}H_{12}F_3OP$, 332.0578; found, 332.0582.

Tris(4-chlorophenyl)phosphine oxide (TClPPO) was isolated as a white solid (108 mg, yield: 89%). mp: 171–172 °C (lit.ref 172–174 °C). ^{1}H NMR ($CDCl_3$, 400 MHz): δ 7.60–7.55 (m, 6H), 7.48–7.44 (m, 6H). ^{13}C NMR ($CDCl_3$, 100 MHz). δ 139.4, 133.7–133.6, 129.4. ^{31}P NMR ($CDCl_3$, 162 MHz): δ 26.9. HRMS (m/z): $[M]^+$ calcd. for $C_{18}H_{12}Cl_3OP$, 379.9691; found, 379.9692.

Tris(4-bromophenyl)phosphine oxide (TBrPPO) was isolated as a white solid (130 mg, yield: 85%). mp: 178–180 °C (lit.ref 179–180 °C). ^{1}H NMR ($CDCl_3$, 400 MHz): δ 7.65–7.62 (m, 6H), 7.52–7.49 (m, 6H). ^{13}C NMR ($CDCl_3$, 100 MHz). δ 133.3, 132.0, 130.6, 127.7. ^{31}P NMR ($CDCl_3$, 162 MHz): δ 27.8. HRMS (m/z): $[M]^+$ calcd. for $C_{18}H_{12}Br_3OP$, 513.8155; found, 513.8158.

Device fabrication

First, the PEDOT: PSS solution was mixed with the PFI solutions at a mass ratio of 1:1 and then filtered for further use. Then, the mixture was spin-coated onto the substrates at 4000 × g for 45 s in the atmosphere, followed by annealing at 150 °C for 30 min. Second, PTAA (5 mg mL^{-1} in chlorobenzene) was spin-coated onto the substrate at 4000 × g for 45 s, followed by annealing at 120 °C for 25 min in a nitrogen-filled glovebox. The emitting layer was fabricated by spin-coating QD

solutions at 2000 × *g* for 45 s. Finally, TPBi (40 nm), LiF (100 nm) and Al (1 nm) were evaporated in sequence under a vacuum of ~2×10^{-4} Pa. The emitting area was 0.15 cm × 0.2 cm. For air-processed QLEDs, we spun PEDOT: PSS: PFI, PTAA and QD solution in the atmosphere at ~25 °C and a relative humidity of 20~30%. The remaining vacuum evaporation steps were the same.

Computational details

The DFT calculations were carried out using the PWmat code[38,39]. The optimised Vanderbilt norm-conserving (OVNC) pseudopotential NCPP-SG15-PBE and PBE functional were adopted under the generalised gradient approximation (GGA)[40–42]. The *k*-mesh and encut were set to 2 × 2 × 2 and 50 Ry for structural optimisation, self-consistent field and projected density of state (PDOS) calculations, respectively. The vacuum level was set to be larger than 15 Å to avoid the interaction between different layers. The Fermi level was set to 0 in all PDOS results.

Characterisation and device measurements

For STEM analysis, the diluted QD solution was dropped onto a carbon-coated Cu grid. STEM was performed applying an aberration-corrected FEI (Themis Z) at 300 kV with a beam current of ~2 pA. PL spectra were collected applying a Varian Cary Eclipse spectrometer (F-7000 FL Spectrophotometer; Excitation light source: xenon lamp; Excitation light wavelength: 405 nm; Scan speed: 240 nm min^{-1}). PL decay measurements were conducted applying a time-correlated single-photon counting (TCSPC) spectrofluorometer (FLS920, Edinburg Instrument, UK). The decay curves were fitted by applying the bi-exponential equation: $I = A_1 \exp\left(-\frac{t}{\tau_1}\right) + A_2 \exp\left(-\frac{t}{\tau_2}\right)$. The average PL lifetime was calculated by: $\tau_{avg} = \frac{A_1\tau_1^2 + A_2\tau_2^2}{A_1\tau_1 + A_2\tau_2}$. XRD patterns were obtained by applying a Bruker D8 Advance X-ray diffractometer with Cu Kα radiation (λ = 1.5406 Å). AFM images were obtained and analysed by applying an Atomic Force Microscope (Cypher ES, Oxford Instruments Asylum Research Inc.). NMR spectra were measured by using a Brucker AVANCE III spectrometer in deuterated chloroform with tetramethyl silane as the internal standard. All the reactions were carried out using Schlenk techniques under nitrogen conditions. For transient absorption spectroscopy, the pump-probe experiments were conducted by using a transient absorption/transmission spectrometer (Helios Fire, Ultrafast Systems). A Ti: Sapphire amplifier (Coherent Inc.) operating at a 1 kHz repetition rate generated infrared pulses (800 nm, 35 fs), which were divided into two beams. The first beam was directed into an optical parametric amplifier (OPA) to produce tunable pump pulses for resonant or near-resonant excitation of the sample. The second beam generated white-light continuum probe pulses through a sapphire plate focusing, with temporal delay controlled by a motorised delay line. Both beams were spatially overlapped in the sample, exhibiting spot diameters of 200 µm (pump) and 6 µm (probe). The transmitted probe signals were detected by a spectrometer equipped with a back-thinned CCD array. Differential transmission ($\Delta T/T$) was calculated as $(T_{on} - T_{off})/T_{off}$, where T_{on} and T_{off} correspond to pump-activated and baseline probe intensities. The EL spectra, *L-J-V* characteristics and EQE were all measured in a nitrogen-filled glovebox at room temperature through an integrated LED testing equipment. The equipment is composed of a Keithley 2400 source, a fibre integration sphere, and a PMA-12 spectrometer, which is designed by Ocean Optics Co., Ltd.

Data availability

The data that support the findings of this study are provided in the main text and the Supplementary Information. More data are available from the corresponding author upon request. Source data are provided with this paper.

References

1. Li, H. et al. Nanosurface-reconstructed perovskite for highly efficient and stable active-matrix light-emitting diode display. *Nat. Nanotechnol.* **19**, 638–645 (2024).
2. Zhao, B. et al. Highly stable perovskite light-emitting diodes. *Matter* **7**, 772–793 (2024).
3. Chiba, T. et al. Anion-exchange red perovskite quantum dots with ammonium iodine salts for highly efficient light-emitting devices. *Nat. Photon.* **12**, 681–687 (2018).
4. Kim, Y.-H. et al. Exploiting the full advantages of colloidal perovskite nanocrystals for large-area efficient light-emitting diodes. *Nat. Nanotechnol.* **17**, 590–597 (2022).
5. Chen, J., Mukherjee, S., Li, W., Zeng, H. & Fischer, R. A. Bespoke crystalline hybrids towards the next generation of white LEDs. *Nat. Rev. Mater.* **7**, 677–678 (2022).
6. Woo, S.-J., Kim, J. S. & Lee, T.-W. Characterisation of stability and challenges to improve lifetime in perovskite LEDs. *Nat. Photon.* **15**, 630–634 (2021).
7. Shamsi, J., Raino, G., Kovalenko, M. V. & Stranks, S. D. To nano or not to nano for bright halide perovskite emitters. *Nat. Nanotechnol.* **16**, 1164–1168 (2021).
8. Akkerman, Q. A., Raino, G., Kovalenko, M. V. & Manna, L. Genesis, challenges and opportunities for colloidal lead halide perovskite nanocrystals. *Nat. Mater.* **17**, 394–405 (2018).
9. Ji, K. et al. Self-supervised deep learning for tracking degradation of perovskite light-emitting diodes with multispectral imaging. *Nat. Mach. Intell.* **5**, 1225–1235 (2023).
10. Chen, J. et al. Nanoscale heterophase regulation enables sunlight-like full-spectrum white electroluminescence. *Nat. Commun.* **16**, 3621–3632 (2025).
11. Yu, Z. et al. Overcoming lattice mismatch for core-shell NaGdF4@CsPbBr3 heterostructures. *Nat. Commun.* **16**, 3891 (2025).
12. Chen, J. et al. Perovskite white light emitting diodes: progress, challenges, and opportunities. *ACS Nano* **15**, 17150–17174 (2021).
13. Li, J. et al. 50-Fold EQE improvement up to 6.27% of solution-processed all-inorganic perovskite CsPbBr3 QLEDs via surface ligand density control. *Adv. Mater.* **29**, 1603885 (2017).
14. Song, J. et al. Room-temperature triple-ligand surface engineering synergistically boosts ink stability, recombination dynamics, and charge injection toward EQE-11.6% perovskite QLEDs. *Adv. Mater.* **30**, e1800764 (2018).
15. Wang, Y. K. et al. All-inorganic quantum-Dot LEDs based on a phase-stabilised alpha-CsPbI(3) perovskite. *Angew. Chem. Int. Ed.* **60**, 16164–16170 (2021).
16. Song, J. et al. Organic-inorganic hybrid passivation enables perovskite QLEDs with an EQE of 16.48. *Adv. Mater.* **30**, e1805409 (2018).
17. Protesescu, L. et al. Nanocrystals of cesium lead halide perovskites (CsPbX(3), X = Cl, Br, and I): novel optoelectronic materials showing bright emission with wide color gamut. *Nano Lett.* **15**, 3692–3696 (2015).
18. Sun, C., Jiang, Y., Zhang, L., Wei, K. & Yuan, M. Toward the controlled synthesis of lead halide perovskite nanocrystals. *ACS Nano* **17**, 17600–17609 (2023).
19. Feng, Y. et al. Nucleophilic reaction-enabled chloride modification on CsPbI3 quantum dots for pure red light-emitting diodes with efficiency exceeding 26%. *Angew. Chem. Int. Ed.* **63**, e202318777 (2024).
20. Chen, X., Huang, J., Gao, F. & Xu, B. Phosphine oxide additives for perovskite light-emitting diodes and solar cells. *Chem* **9**, 562–575 (2023).
21. Xu, L. et al. A bilateral interfacial passivation strategy promoting efficiency and stability of perovskite quantum dot light-emitting diodes. *Nat. Commun.* **11**, 3902 (2020).

22. Xue, J., Wang, R. & Yang, Y. The surface of halide perovskites from nano to bulk. *Nat. Rev. Mater.* **5**, 809–827 (2020).
23. Yang, X. et al. Efficient green light-emitting diodes based on quasi-two-dimensional composition and phase engineered perovskite with surface passivation. *Nat. Commun.* **9**, 570 (2018).
24. Ma, D. et al. Distribution control enables efficient reduced-dimensional perovskite LEDs. *Nature* **599**, 594–598 (2021).
25. Jiang, J. et al. Efficient pure-red perovskite light-emitting diodes with strong passivation via ultrasmall-sized molecules. *Sci. Adv.* **10**, eadn5683 (2024).
26. Chen, J. et al. Molecule-induced ripening control in perovskite quantum dots for efficient and stable light-emitting diodes. *Sci. Adv.* **11**, eado7159 (2025).
27. Cai, B. et al. A new descriptor for complicated effects of electronic density of states on ion migration. *Adv. Funct. Mater.* **33**, 2300445 (2023).
28. Chen, S. et al. Atomic-scale insights into surface instability in halide perovskites. *Nano Lett.* **24**, 15363–15370 (2024).
29. Chen, J. et al. Efficient and bright white light-emitting diodes based on single-layer heterophase halide perovskites. *Nat. Photon.* **15**, 238–244 (2021).
30. Yao, J. S. et al. Few-nanometer-sized alpha-CsPbI3 quantum dots enabled by strontium substitution and iodide passivation for efficient red-light emitting diodes. *J. Am. Chem. Soc.* **141**, 2069–2079 (2019).
31. Guo, Z. et al. Promoting energy transfer via manipulation of crystallization kinetics of quasi-2D perovskites for efficient green light-emitting diodes. *Adv. Mater.* **33**, e2102246 (2021).
32. Luo, X. et al. Ultrabright blue lead-halide perovskite light-emitting diodes based on phosphonic acid functionalized hole injection layer. *ACS Nano* **19**, 16850–16858 (2025).
33. Cheng, Y. et al. Air-processed perovskites enabled by an interface-reconstruction strategy for high-performance light-emitting diodes. *Nano Lett.* **25**, 6192–6199 (2025).
34. Li, M. et al. Trade-off between efficiency and stability of CsPbBr3 perovskite quantum dot-based light-emitting diodes by optimized passivation ligands for Br/Pb. *Adv. Funct. Mater.* **34**, e2308341 (2023).
35. Guo, B. et al. Ultrastable near-infrared perovskite light-emitting diodes. *Nat. Photon.* **16**, 637–643 (2022).
36. Kong, L. et al. Fabrication of red-emitting perovskite LEDs by stabilising their octahedral structure. *Nature* **631**, 73–79 (2024).
37. Wang, Y. K. et al. Long-range order enabled stability in quantum dot light-emitting diodes. *Nature* **629**, 586–591 (2024).
38. Jia, W. et al. Fast plane wave density functional theory molecular dynamics calculations on multi-GPU machines. *J. Comput. Phys.* **251**, 102–115 (2013).
39. Jia, W. et al. The analysis of a plane wave pseudopotential density functional theory code on a GPU machine. *Comput. Phys. Commun.* **184**, 9–18 (2013).
40. Hamann, D. Optimised norm-conserving Vanderbilt pseudopotentials. *Phys. Rev. B* **88**, 085117 (2013).
41. Schlipf, M. & Gygi, F. Optimization algorithm for the generation of ONCV pseudopotentials. *Comput. Phys. Commun.* **196**, 36–44 (2015).
42. Perdew, J. P., Burke, K. & Ernzerhof, M. Generalised gradient approximation made simple. *Phys. Rev. Lett.* **77**, 3865 (1996).

Acknowledgements

This work was financially supported by the the National Key Research and Development Program of China (2024YFB3612400, H.Z.), National Natural Science Foundation of China (52203229, D.M.; U24A20286, H.Z.; 62261160392, H.Z.; 62504114, J.C.; 62404107, B.C.; 62204120, Q.S.), the Tsinghua University Initiative Scientific Research Program (Tsinghua University Dushi Program, D.M.), the Natural Science Foundation of Jiangsu Province (Grant BK20220396, B.C.), the Natural Science Foundation of Hunan Province (2024JJ4005, S.C.), International Cooperation Program (BZ2024038, H.Z.) of Jiangsu Province of China, the China Postdoctoral Science Foundation (2023M741916, J.C.; 2024T170466, J.C.) and the Postdoctoral Fellowship Program of CRSF (GZB20230332, J.C.).

Author contributions

J.C. conceived the device design and experiments. J.C. carried out most of the material synthesis and device construction. Xiangyu L. synthesised organic molecules and performed NMR measurements. B.C. and X.Y. performed theoretical calculations and analysed the results. H.W., B.X., and Linjie D. performed transient absorption spectroscopy and analysed the results. Y.C. D.Z. J.D. performed optical measurements. Y.X. performed TEM measurement under the supervision of S.C. Xiyu L., W.F., S.D., and Q.S. helped analyse device data. J.C. wrote the manuscript. D.M., H.Z., and Lian D. assisted J.C. in polishing the manuscript. All the authors discussed and commented on the results.

Competing interests

The authors declare no competing interests.

Additional information

Supplementary information The online version contains supplementary material available at https://doi.org/10.1038/s41467-025-63684-9.

Correspondence and requests for materials should be addressed to Lian Duan or Dongxin Ma.

Peer review information *Nature Communications* thanks Xingliang Dai and the other anonymous reviewer(s) for their contribution to the peer review of this work. A peer review file is available.